Pergamon

Int. J. Heat Mass Transfer. Vol. 37, No. 14, pp. 2101–2111, 1994

0017-9310/94 $7.00 + 0.00

0017-9310(94)E0036-T

Thermal stability of a diathermanous fluid in a multi-layer system with partially transparent radiating boundaries

R. F. RICHARDS

Department of Mechanical and Materials Engineering, Washington State University, Pullman, WA 99164-2920, U.S.A.

(*Received* 24 *May* 1993 *and in final form* 13 *January* 1994)

Abstract—The thermal stability of a diathermanous, thermally-expansive fluid, divided into parallel horizontal layers by partially transparent barriers, and heated from below is considered. The effects of horizontal conduction within and radiative coupling between the intermediate barriers as well as the ratios of individual fluid layer thicknesses on critical Rayleigh number are predicted using linear stability theory. The results of the analysis are confirmed experimentally for double and triple air layers separated by plastic sheets.

INTRODUCTION

To SUPPRESS convective heat loss from a flat plate solar collector one or more transparent covers may be interposed between the absorber and the environment. Whillier [1] considered the use of thin plastic sheets as multiple glazings for solar collectors. He used a one-fourth power law to approximate convective heat transfer across the air gaps. Hollands and Wright [2] repeated the analysis of Whillier [1] more rigorously, using a correlation reported by Hollands *et al.* [3] for convective heat transfer across single fluid layers enclosed between isothermal boundaries. Measurements made by Hollands and Wright [2] for heat transfer across an air layer divided in two by a 1 mm Teflon sheet demonstrated the shortcomings of this approach; measured heat flux exceeded predictions by more than 20%. The difference was attributed to the fact that the Teflon sheet dividing the two air layers would not form an isothermal boundary. Edwards and Rhee [4] analysed the case of a flat plate collector with inner glazings of either plastic film or glass. They took into account the non-isothermality of the inner barrier by incorporating the linear stability analysis of Sparrow *et al.* [5] for single layers with boundaries of finite conductivity. Gershuni and Zhukhovitskii [6] gave an approximate solution for the critical Rayleigh number of a fluid layer with outer isothermal boundaries and divided in half by a horizontal barrier of finite thickness and conductivity. Catton and Lienhard [7] analysed the same situation using the Galerkin method but allowed the intermediate barrier to be located at any position between the outer boundaries. Fluid property temperature dependence and radiative coupling were neglected in the analysis. Under these conditions the most stable arrangement was shown to occur when the ratio of fluid layer thicknesses was equal to 1.

Lienhard and Catton [8] calculated heat transfer across a double layer with a centrally located intermediate barrier applying power integral theory. They found it was possible to correlate their results with the dimensionless conduction ratio $(K_f L_b)/(K_b(L_1+L_2)$ when the ratio $aL_b/(L_1+L_2)$ is small. Thermal conductivities K_f and K_b are for the fluid and the intermediate barrier, respectively. Thicknesses L_1, L_2 and L_b are for the two fluid layers and the intermediate barrier, respectively, and a is the dimensionless perturbation wavenumber. A comparison of their predictions with the heat transfer measurements of Hollands and Wright [2] and Ulrich [9] showed good agreement.

Lienhard [10] calculated critical Rayleigh numbers for two, three and four fluid layer systems by extending the analysis of Catton and Lienhard [7]. Hieber [11] demonstrated how a shooting algorithm could be applied to multi-layer stability problems, considerably simplifying the numerical solution.

Richards and Edwards [12] showed the stabilizing effect of boundary radiation on the thermal stability of single and double fluid layer systems where the fluid is diathermanous. The analysis of the double layer system required the two layers to be of equal thickness but allowed the intermediate barrier to be partially transparent with arbitrary emissivity and reflectivity. Lienhard [13] also investigated the effect of boundary radiation on the double layer. His treatment allowed fluid layers of unequal thickness, but was restricted to the case of an opaque intermediate barrier.

The present work involves a more general analysis of the multi-layer stability problem with radiation, allowing both arbitrary fluid layer thickness ratios and partially transparent barriers. The situation considered is that of n horizontal layers of diathermanous, thermally-expansive fluid, separated by $(n-1)$ par-

NOMENCLATURE

a	perturbation wavenumber
B	black body radiosity
Bi	Biot number
D_z	z-derivative
F_{ij}	perturbation transfer factor
g	gravitational acceleration
Gr	Grashof number
h	heat transfer coefficient
H	barrier or boundary to fluid layer conductance ratio
F_{ij}	mean transfer factor
K	conductivity
L	fluid layer thickness
n	number of fluid layers
Nu	Nusselt number
Pr	Prandtl number
q	heat flux
Ra	Rayleigh number
R_{ij}	heat flux ratio
$S(a)$	shape factor attenuation factor
T	temperature
t	barrier or boundary thickness
$W(z)$	z-velocity component z-dependence
x	horizontal coordinate
z	vertical coordinate.

Greek symbols

α	thermal diffusivity
β	volume coefficient of expansion
δ	amplitude of radiosity/irradiation perturbation
ΔT	temperature difference
ε	emissivity
$\theta(z)$	temperature perturbation z-dependence
λ	fluid-layer thickness ratio
μ	dynamic viscosity
ν	kinematic viscosity
ρ	reflectivity
σ	Stefan–Boltzmann constant
τ	transmissivity.

Subscripts

b	outer boundary or intermediate barrier
c	conductive/convective
cr	critical
f	fluid
i	individual fluid layer i
M	mean
max	maximum
r	radiative
tot	total system
ν	spectral.

Superscripts

$+/-$	radiosity/irradiation
$\bar{}$	mean quantity
$'$	perturbation
*	dimensional quantity.

tially transparent intermediate barriers with arbitrary emissivity, reflectivity and thermal conductivity. Critical Rayleigh numbers are presented for the particular cases of two and three fluid layers. Experimental measurements of heat flux across double and triple air layers separated by plastic sheets are also reported and compared with the predictions of the linear stability analysis.

THEORY

A diathermanous, thermally-expansive fluid is divided into n horizontal layers of arbitrary thickness as shown in Fig. 1. If an adverse temperature gradient of sufficient magnitude is imposed by heating the bottom and cooling the top of the multi-layer system, then the enclosed fluid may become unstable to small disturbances in temperature and velocity. The stability of the system may be analysed by assuming small perturbations of temperature about the mean or quiescent base state temperature gradient. The perturbed temperature profile in the ith layer is assumed to take the form:

$$T(x_i, z_i) = \bar{T}(z_i) + T'(x_i, z_i), \tag{1}$$

where

$$T'(x_i, z_i) = (\Delta T_i)\theta(z_i)\cos(a_i x_i), \tag{2}$$

and where x_i and z_i are the horizontal and vertical cartesian coordinates, non-dimensionalized by the ith fluid layer thickness, L_i. The linearized time-independent perturbation equations governing these

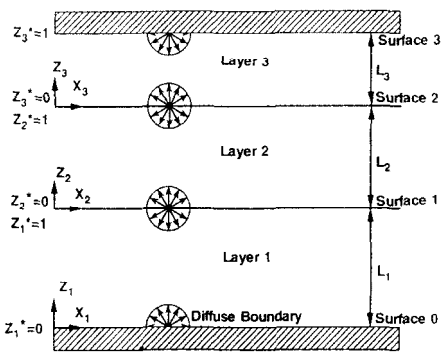

FIG. 1. The n-layer system ($n = 3$).

infinitesimal disturbances within each individual fluid layer may then be written as [14]:

$$(D_z^2 - a_i^2)\theta(z_i) = -Pr_i W(z_i), \tag{3}$$

$$(D_i^2 - a_i^2)^2 W(z_i) = a_i^2 Gr_i \theta(z_i), \tag{4}$$

such that:

$$(D_z^2 - a_i^2)^3 \theta(z_i) = -a_i^2 Ra_i \theta(z_i). \tag{5}$$

Here $\theta(z_i)$ and $W(z_i)$ are the temperature and the z-velocity component perturbations non-dimensionalized by ΔT_i and ν_i/L_i, respectively. Operator D_z is the z-derivative, and a_i is the disturbance wavenumber, both non-dimensionalized with respect to L_i. The subscript i identifies the individual fluid layer within the multi-layer stack.

Two sets of dimensionless numbers are defined. The individual fluid layer Rayleigh number, Grashof number, and Prandtl number in equations (4)–(6) are defined to be:

$$Ra_i = Gr_i Pr_i \quad Gr_i = g\beta_i \Delta T_i L_i^3/\nu_i^2 \quad Pr_i = \nu_i/\alpha_i, \tag{6}$$

where ΔT_i is the temperature drop across the ith fluid layer, and β_i, α_i, and ν_i are evaluated at the mean temperature of the ith layer. Total Rayleigh, Grashof, and Prandtl numbers are also defined:

$$Ra_{\text{tot}} = Gr_{\text{tot}} Pr_{\text{tot}} \quad Gr_{\text{tot}} = g\beta\Delta T L^3/\nu^2 \quad Pr_{\text{tot}} = \nu/\alpha, \tag{7}$$

where ΔT is the total temperature drop across all layers and β, α, and ν are evaluated at the mean temperature of the entire stack.

The boundary conditions on velocity for each layer are zero velocity and (from continuity) zero first derivative of W:

$$W(z_i) = 0 \quad z_i = 0, 1 \tag{8}$$

$$D_z W|_{z_i} = 0 \quad z_i = 0, 1. \tag{9}$$

The thermal boundary conditions imposed are continuity in temperature across each intermediate barrier (assuming negligible thermal resistance across the barriers), and continuity in heat flux at every boundary. The first condition, continuity in temperature, is:

$$\theta(z_i = 1) = \theta(z_{(i+1)} = 0). \tag{10}$$

The second condition, continuity in heat flux, is developed by applying heat flux balances at the two outer boundaries, and at each intermediate barrier. Both intermediate barriers and outer boundaries are treated by invoking the fin approximation, so that horizontal conduction within each barrier or boundary is accounted for. Equation (1) is then substituted into the total heat balances on the fin-like boundaries and barriers. Subtracting out similarly developed mean or quiescent-base-state heat balances from the total heat balances gives temperature perturbation boundary conditions at the upper and lower outer boundaries, and at the ith intermediate barrier:

$$-h_n T'(z_n^* = L_n) = K_{\text{f},n} \left.\frac{\partial T'}{\partial z^*}\right|_{z_n^* = L_n} - K_{\text{b},n} t_n \frac{\partial^2 T'}{\partial x^{*2}} + q'_{\text{r},n}, \tag{11}$$

$$-h_0 T'(z_1^* = 0) = -K_{\text{f},1} \left.\frac{\partial T'}{\partial z^*}\right|_{z_1^* = 0} - K_{\text{b},0} t_0 \frac{\partial^2 T'}{\partial x^{*2}} + q'_{\text{r},0}, \tag{12}$$

$$-K_{\text{f},i} \left.\frac{\partial T'}{\partial z^*}\right|_{z_i^* = L_i} = -K_{\text{f},(i+1)} \left.\frac{\partial T'}{\partial z^*}\right|_{z_{(i+1)}^* = 0} - K_{\text{b},i} t_i \frac{\partial^2 T'}{\partial x^{*2}} + q'_{\text{r},i}. \tag{13}$$

The starred symbols, x^* and z^*, are the horizontal and vertical cartesian coordinates in dimensional form. The symbol $K_{\text{f},i}$ designates the ith fluid layer conductivity, while $K_{\text{b},i}$ and t_i are the conductivity and thickness of ith boundary or barrier. The perturbations to the mean radiative flux at each boundary, designated $q'_{\text{r},i}$, can be expressed in terms of the perturbations to the mean black-body radiosity of each surface and the transfer factors from surface to surface. The spectral black body radiosity from the ith surface can be expressed as:

$$B_{\nu,i} = B_\nu[\bar{T}(z_i = 0)] + T'(x, 0) \left.\frac{\partial B_\nu}{\partial T}\right|_{T = \bar{T}(z_i = 0)}, \tag{14}$$

in order to make use of the assumed form of the small perturbations in temperature at each boundary [equation (2)]. Richards and Edwards [12] previously showed that a radiosity in the form of a mean value plus a sinusoidally varying perturbation from boundary i,

$$q^+_{\nu,i}(x) = \bar{q}^+_{\nu,i} + \delta_{\nu,i} \cos(ax^*). \tag{15}$$

will result in an irradiation of a similar form on the facing boundary, j,

$$q^-_{\nu,j}(x) = \bar{q}^+_{\nu,i} + S(a)\delta_{\nu,i} \cos(ax^*). \tag{16}$$

The function $S(a)$ is the spatial attenuation factor and was given in Fig. 2 of Richards and Edwards [12]. In that paper the spatial attenuation factor was shown to act like a geometric transmissivity, attenuating perturbation radiation as it crossed a fluid layer.

The transfer factors for perturbation radiation from one surface to another may be determined algebraically using the radiosity–irradiation equations. The case of a single layer (to which the situation of multiple layers reduces when all barriers are opaque to thermal radiation) and the case of twin symmetric layers with a specularly reflecting and transmitting intermediate barrier have already been dealt with. The more general case of n arbitrary layers with $(n-1)$ semi-transparent intermediate barriers and two outer boundaries is considered here.

For an n-layer stack the algebra leads to:

$$q'_{r,i} = F_i B'_i + \sum_{j=0}^{n} F_{i,j}(B'_i - B'_j), \tag{17}$$

where the $F_{i,j}$ are the perturbation transfer factors from surface i to surface j. For convenience, both sides of each intermediate barrier are taken to be part of the same surface. Integration of spectral values over all photon wavenumbers to arrive at total values is implied by the disappearance of the subscript ν in equation (17). The new transfer factor introduced here, F_i, represents the fraction of perturbation radiation emitted by the ith surface and not absorbed by any surface. This radiation is 'lost' due to the geometrical averaging or attenuation accounted for by $S(a)$. It follows then that a perturbation radiant heat balance on any surface i must lead to the identity:

$$\varepsilon_i = F_i + \sum_{j=0}^{n} F_{i,j}. \tag{18}$$

Substituting equation (14) into (17), making use of (18), yields:

$$q'_{r,o} = \varepsilon_o h_{r,o} T'(z_1^* = 0) - F_{o,o} h_{r,o} T'(z_1^* = 0) - \sum_{j=1}^{n} F_{o,j} h_{r,j} T'(z_j^* = L_j), \tag{19}$$

for the net perturbation radiant heat flux from the lower boundary in terms of the temperature perturbations, and:

$$q'_{r,i} = \varepsilon_i h_{r,i} T'(z_i^* = L_i) - F_{i,o} h_{r,o} T'(z_1^* = 0) - \sum_{j=1}^{n} F_{i,j} h_{r,j} T'(z_j^* = L_j), \tag{20}$$

for all other surfaces. The radiation heat transfer coefficients, $h_{r,o}$ and $h_{r,i}$, are defined to be:

$$h_{r,o} = 4\sigma \bar{T}^3(z_1^* = 0) \quad h_{r,i} = 4\sigma \bar{T}^3(z_i^* = L_i). \tag{21}$$

Introducing equations (19) and (20) into (11)–(13), and non-dimensionalizing gives the final form of the thermal boundary conditions for the upper, lower and intermediate boundaries as:

$$D_z\theta|_{z_1=0} = (Bi_{c,o} + a_1^2 H_o + \varepsilon_o Bi_{r,o})\theta(z_1 = 0) - F_{o,o} Bi_{r,o}\theta(z_1 = 0) - \sum_{j=1}^{n} F_{o,j} Bi_{r,j} R_{j,1}\theta(z_j = 1) \tag{22}$$

$$-D_z\theta|_{z_n=1} = (Bi_{c,n} + a_n^2 H_n + \varepsilon_n Bi_{r,n})\theta(z_n = 1) - F_{n,o} Bi_{r,o} R_{1,n}\theta(z_1 = 0) - \sum_{j=1}^{n} F_{n,j} Bi_{r,j} R_{j,n}\theta(z_j = 1) \tag{23}$$

$$-D_z\theta|_{z_i=1} + R_{(i+1),i} D_z\theta|_{z_{(i+1)}=0} = (a_i^2 H_i + \varepsilon_i Bi_{r,i})\theta(z_i = 1) - F_{i,o} Bi_{r,o} R_{1,i}\theta(z_1 = 0) - \sum_{j=1}^{n} F_{i,j} Bi_{r,j} R_{j,i}\theta(z_j = 1), \tag{24}$$

where convective and radiative Biot numbers are defined to be:

$$Bi_{c,o} = \frac{h_{c,o} L_1}{K_{f,1}} \quad Bi_{c,i} = \frac{h_{c,i} L_i}{K_{f,i}}$$

$$Bi_{r,o} = \frac{h_{r,o} L_1}{K_{f,1}} \quad Bi_{r,i} = \frac{h_{r,i} L_i}{K_{f,i}}. \tag{25}$$

The quantities H and R_{ij} are the barrier to fluid-layer conductance ratio and the individual heat flux ratio:

$$H_o = \frac{K_{b,i} t_o}{K_{f,1} L_1} \quad H_i = \frac{K_{b,i} t_i}{K_{f,i} L_i} \quad R_{ij} = \frac{K_i \Delta T_i L_j}{K_j \Delta T_j L_i}. \tag{26}$$

The barrier to fluid-layer conductance ratio, H, parameterizes horizontal conduction in the intermediate barriers and outer boundaries. The heat flux ratio, $R_{i,j}$, which characterizes conduction heat tranfer across individual fluid layers, varies from unity because of radiative interactions.

METHOD OF SOLUTION

The solution of the multi-layer linear stability problem posed in equations (3)–(5), (8)–(10) and (22)–(24) requires the specification of the base, quiescent state of the multi-layer stack. To establish the temperatures of each of the intermediate boundaries (and the resulting temperature gradients across each individual fluid layer) an iterative relaxation scheme is used. The temperature of the ith intermediate boundary is found by applying heat balances on each of the ith intermediate barriers, taking into account conduction through fluid layers and surface-to-surface radiation between barriers.

Perturbation transfer factors $F_{i,j}$ are found using the plating algorithm developed by Edwards [15]. The stack of fluid layers is considered as an enclosure, with the outer boundaries and the intermediate barriers acting as the surfaces of the enclosure. All surfaces are taken to be diffuse emitters and reflectors. Calculation of the transfer factors for the stack requires a minor modification to the recursion relations (10)–(13) given in Edwards [15] because the transmissivity of the intermediate barriers and the action of the spatial attenuation factor must be taken into account. In the present application the four cases become:

Case 1. $(i \neq k, j \neq k)$

$$F_{i,j}^* = F_{i,j} + \frac{1}{D_k} \frac{\rho_k}{(1-\tau_k)^2} F_{i,k} F_{k,j}, \tag{27a}$$

Case 2. $(i \neq k, j = k)$

$$F_{i,k}^* = \frac{1}{D_k} \frac{\varepsilon_k}{(1-\tau_k)} F_{i,k}, \tag{27b}$$

Case 3. $(i = k, j \neq k)$

$$F^*_{k,j} = \frac{1}{D_k}\frac{\varepsilon_k}{(1-\tau_k)}F_{k,j}, \tag{27c}$$

Case 4. $(i = k, j = k)$

$$F^*_{k,k} = \frac{1}{D_k}\frac{\varepsilon_k^2}{(1-\tau_k)^2}F_{k,k}, \tag{27d}$$

where

$$D_k = 1 - \frac{\rho_k F_{k,k}}{(1-\tau_k)^2}. \tag{27e}$$

The starting values of $F_{i,j}$ chosen for the recursion relations (27a) (27c) will be the transfer factors for a stack with opaque outer boundaries, intermediate barriers with the given transmissivity, no reflectivity, and the corresponding emissivity $(\varepsilon = 1-\tau)$ and which also include the effect of $S(a)$. Under these assumptions the transfer factors are easily formulated:

$$F_{i,j} = \varepsilon_i\varepsilon_j S(a_{i,j})\prod_{k=(i+1)}^{(j-1)}\tau_k, \tag{28}$$

where $a_{i,j}$ is the perturbation wavenumber non-dimensionalized with respect to the length L_{ij} between surfaces i and j:

$$L_{ij} = \sum_{k=(i+1)}^{j} L_i. \tag{29}$$

Given the intra-stack transfer factors and the temperatures of the intermediate barriers for the multi-layer system's base state, the linear stability problem may be solved. The shooting method of Hieber [11] is employed. For each of the n layers in the stack, equation (5) is applied. The sixth-order ordinary differential equation is broken down into a system of six first-order equations, the solution of which is expressed as a linear combination of six independent functions. Six additional boundary conditions are imposed at $z_i = 0$ in each layer in order to recast the original boundary-condition problem as an initial-condition problem. The system of equations is then integrated across each layer from $z_i = 0$ to 1 using a Runge–Kutta routine and the boundary conditions (8)–(10) and (22)–(24) imposed. The result is a system of $4n$ equations in $4n+1$ unknowns, where the $(n+1)$th unknown is Ra_{tot}. The Rayleigh number of neutral stability for a given perturbation wavenumber will be the value which forces the determinant of the system of $4n$ equations to zero. The critical Rayleigh number is the minimum of the curve of Rayleigh number of neutral stability vs perturbation wavenumber.

Hieber [11] was able to solve the stability problem for multi-layer systems by finding the determinant of a 4×4 matrix because he neglected radiation. In the present application a $4n\times4n$ matrix is required, because surface-to-surface radiation causes boundaries not adjacent to one another to become coupled through the heat-flux boundary conditions (22)–(24).

EXPERIMENT

Heat transfer measurements were made with a test cell which served to contain horizontal layers of air while heating the layers from below and cooling them from above. The lower boundary of the test cell is an electrically heated aluminum plate, and the upper boundary is a water-cooled brass plate, both 45×22 cm. Temperatures of the aluminum hot plate and the brass cold plate are monitored with type E thermocouples. Phenolic spacers and paperboard walls placed around the periphery of the test cell make up its sidewalls. First-surface aluminized mylar completely covers the sidewalls of the test cell so that, with the barbershop mirror effect, it behaves radiatively as if it were infinite in the horizontal plane. The vertical thickness of each air layer is determined by the phenolic spacers. Stacked atop one another, the spacers hold plastic sheets or films which divide the air gap into individual horizontal layers. The entire test cell is enclosed in a pressure vessel which can be evacuated down to 1 Torr or pressurized up to 1500 Torr absolute, allowing precise control of the pressure.

Heat flux across the air layers is measured using a guard-heated calorimeter. The calorimeter, 40 cm long and 10 cm wide, is mounted into a recess machined into the front face of the aluminum hot plate. Fitting flush with the face of the hot plate, the calorimeter is made up of a brass back plate, a cork inner layer, an inconel-foil resistive heating element, and a copper face sheet. The brass back plate is in good thermal contact with the aluminum hot plate, while the copper face sheet forms the central part of the test cell's lower heated boundary. An eight-junction thermopile (type E) bridging the cork inner layer measures the temperature difference between the copper face plate and the brass base plate of the calorimeter. When the signal from this thermopile is nulled, all electrical power dissipated as heat in the calorimeter's resistance foil heater is transferred out the front of the calorimeter's copper face sheet into the test cell. In this way, measuring the electrical dissipation in the calorimeter heater gives a direct measure of heat transfer across the enclosed air layers.

An experimental run begins by adjusting the air pressure in the test cell until the air-layer system is below its critical Rayleigh number. Rayleigh number is swept from low to high by increasing the test cell air pressure. Heat-flux data are taken at incrementally higher pressures until the particular air-layer system's Nusselt number increases significantly above the quiescent, base-state value for the system. During an experimental run, the cold- and hot-plate temperatures remain constant. Consequently, the contribution of radiative heat transfer to the total heat transfer across the air layers remains constant even as Ra increases.

Heat transfer measurements were made on nine test cases, including single, double, and triple air layers. Those cases are listed in Table 1. The thermophysical

Table 1. Test cases

Case number	Number of layers	Type of barrier	L_1 (mm)	L_2 (mm)	L_3 (mm)	ΔT_{tot} (K)	$T_{M,tot}$ (K)
1	1	—	21.9	—	—	—	—
2	2	Phenolic	13.2	12.4	—	24.9	304.9
3	2	Phenolic (aluminized)	13.2	12.4	—	25.7	311.0
4	2	Mylar	13.2	12.5	—	21.4	308.2
5(a–d)	2	Teflon	13.3	12.5	—	†	‡
6	2	Polyethylene	9.3	12.5	—	20.8	307.6
7	3	Polyethylene	9.4	12.7	8.2	29.8	313.1
8	3	Mylar	9.4	9.3	9.0	19.9	306.0
9	3	Phenolic	9.4	9.3	9.0	21.5	307.3

†(5a) 15.5 K; (5b) 21.1 K; (5c) 24.2 K; (5d) 27.8 K.
‡(5a) 303.6 K; (5b) 306.6 K; (5c) 309.8 K; (5d) 311.4 K.

properties of the plastic sheets used as intermediate barriers in the nine test cases are given in Table 2.

Properties of air used to calculate the experimental Nusselt and Rayleigh numbers are taken from Vargaftik [17]. Air properties used for the Nusselt number and the total Rayleigh number are evaluated at the mean temperature of the hot and cold plates. The temperatures of the plastic sheets serving as intermediate barriers in the multi-layer systems were not measured; thus the air properties used to calculate Nusselt and Rayleigh numbers for an individual layer had to be evaluated at the predicted mean temperature of that layer.

A detailed error analysis of the experiment is given in Richards [16]. The uncertainty of the measured Nusselt number is estimated to be $\pm 2\%$. The uncertainty in measured total Rayleigh number is estimated to be $\pm 3\%$.

RESULTS

Heat-transfer measurements

Figure 2 shows plots of heat-transfer measurements around the onset of instability for four test cases: a single layer (test-case 1), a double layer with a phenolic intermediate barrier (test-case 2), a double layer with a polyethylene intermediate barrier (test-case 6), and a triple layer with two Mylar intermediate barriers (test-case 8). The data shown are typical of the measurements made for each of the nine test cases run. The figure shows plots of Nusselt number as a function of total system Rayleigh number. Solid lines through the data in each figure represent the average Nusselt number of the low-Rayleigh (subcritical) data and a least squares fit to the high-Rayleigh-number (supercritical) data. The intersection of the two lines is taken as the location of the critical Rayleigh number. The onset of instability is unmistakable in the plots.

In the test cases shown, the average subcritical Nusselt number is greater than 1. The difference between the measured subcritical Nusselt numbers and unity can be attributed to radiative transfer across the air layers. As pointed out earlier, the contribution of radiative heat transfer to the total heat transfer across the air layers was constant during each experiment. For this reason, for data in the vicinity of Ra_{cr}, the contribution of radiation heat transfer can be subtracted out of the overall heat transfer, to good approximation, simply by translating the experimental data down until the average of the subcritical measurements falls on the line $Nu = 1$.

The repeatability of the heat-transfer measurements can be gauged by an inspection of data for test-case 2 (Fig. 2b). That plot shows data taken in two separate experimental runs with data from the first run plotted as open squares and data from the second run as open circles. The scatter in the measurements is small, in the order of 2–3%. This level of repeatability is typical of the experimental runs and agrees well with the uncertainty analysis of Richards [16].

Table 3 lists critical Rayleigh numbers and average

Table 2. Thermophysical properties of plastic sheets and films

Plastic sheet or film	Thickness (μm)	k (W m K^{-1})	ε	ρ	τ	H double layer†
Phenolic	760	0.50	0.90	0.10	0.00	1.2
Phenolic (aluminized)	960	0.44‡	0.04	0.96	0.00	1.4
Mylar	25.0	0.16	0.57	0.14	0.29	0.013
Teflon	25.0	0.24	0.38	0.08	0.54	0.020
Polyethylene	13.0	0.33	0.08	0.10	0.82	0.013

†Values for H listed are for double-layer test cases only.
‡Conductivity is a cross-sectional-area weighted average of phenolic and aluminized mylar conductivities.

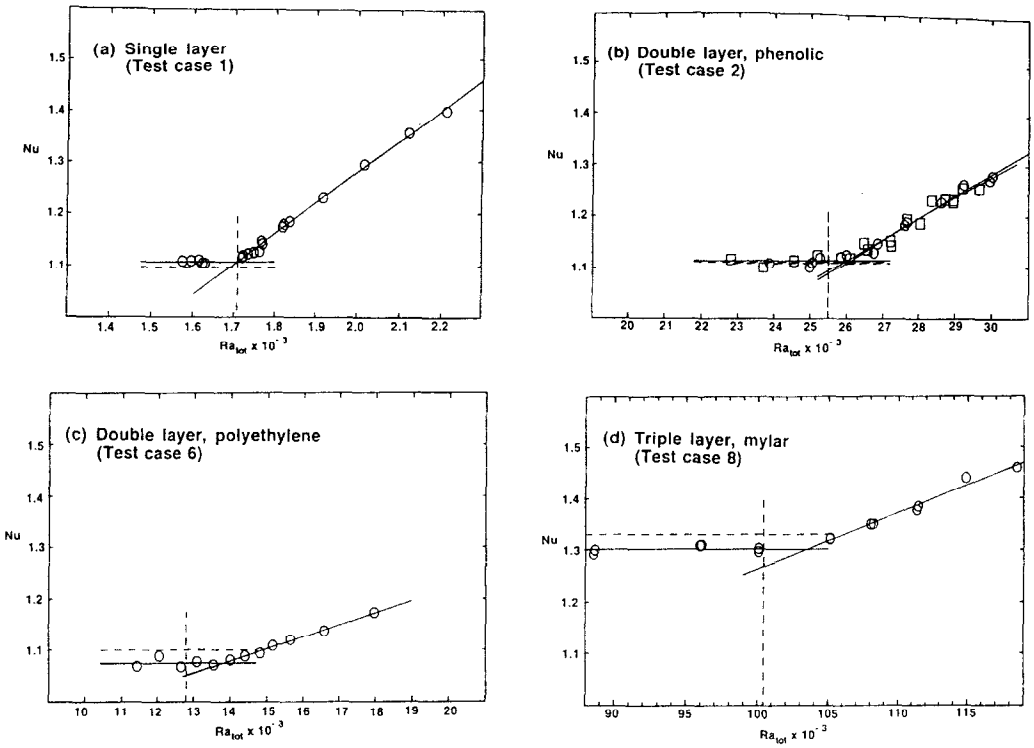

FIG. 2. Heat transfer data for: (a) single layer (test-case 1); (b) double layer with phenolic intermediate barrier (test-case 2); (c) double layer with polyethylene intermediate barrier (test-case 6); (d) triple layer with Mylar intermediate barriers (test-case 8).

subcritical Nusselt numbers determined for each of the nine test cases, using plots similar to those given in Fig. 2.

Linear stability predictions

Critical Rayleigh numbers predicted by the linear stability analysis and subcritical Nusselt numbers predicted by the iterative relaxation scheme are listed in Table 3 along side the experimental values. The critical Rayleigh numbers and subcritical Nusselt numbers given were calculated for each test case based on the information given in Tables 1 and 2. The critical Rayleigh numbers and subcritical Nusselt numbers predicted from theory for test-cases 1, 2, 6 and 8 are also shown by vertical and horizontal dashed lines in Fig. 2.

Figures 3, 4, and 5 illustrate trends in the stability of multi-layer fluid systems predicted by the linear stability theory. The figures show the behavior of individual-layer and total-system critical Rayleigh num-

Table 3. Comparison of theory and experiment

	Subcritical Nusselt number			Critical Rayleigh number $\times 10^{-3}$				
Case	Experiment	Theory	% Error	Experiment	Theory†	% Error	Theory‡	% Difference§
1	1.11	1.10	−1	1.71	1.708	<1	1.708	0
2	1.11	1.11	<1	26.1	25.5	−2	25.0	−2
3	1.05	1.06	+1	25.9	25.0	−4	25.0	<1
4	1.09	1.11	+2	23.9	23.3	−2	20.8	−11
5a	1.08	1.11	+3	23.4	22.5	−4	20.7	−8
5b	1.09	1.11	+2	22.6	22.7	+1	20.9	−8
5c	1.11	1.11	<1	23.8	22.8	−4	20.9	−8
5d	1.10	1.12	+2	23.2	22.8	−2	20.9	−8
6	1.07	1.10	+3	13.8	12.8	−8	12.6	−2
7	1.16	1.21	+4	49.2	48.5	−2	46.9	−3
8	1.30	1.33	+2	104	100	−3	94.4	−6
9	1.34	1.37	+2	104	104	<1	104	<1

†Linear stability theory including radiation.
‡Linear stability theory neglecting radiation.
§Per cent difference between theory including radiation and theory neglecting radiation.

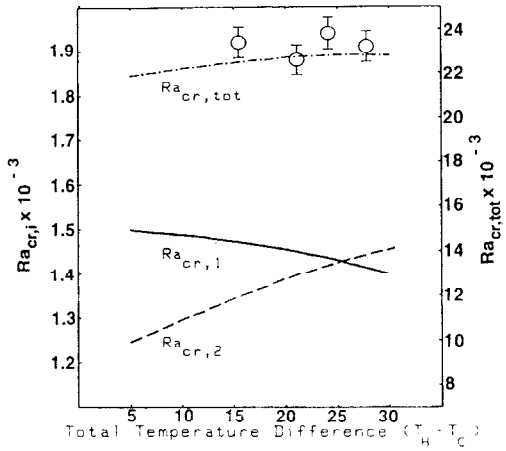

FIG. 3. Predicted total-system and individual-layer critical Rayleigh numbers vs total-system temperature difference for a double-air-layer system with Teflon intermediate barrier, along with experimental data from test case 5.

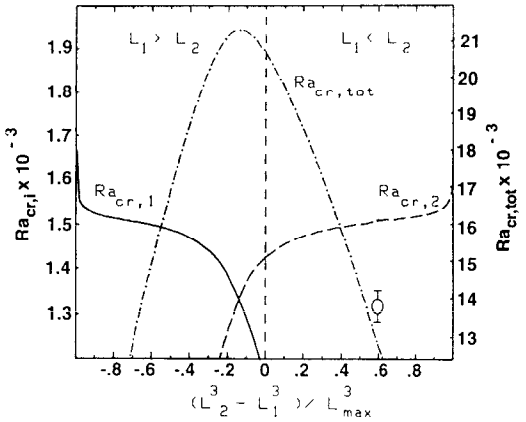

FIG. 4. Predicted total-system and individual-layer critical Rayleigh numbers vs fluid-layer thickness ratio, λ, for a double-air-layer system with polyethylene intermediate barrier, along with experimental datum from test case 6 ($\lambda = 0.59$).

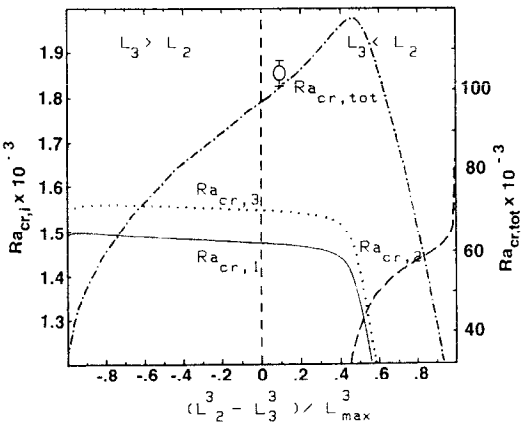

FIG. 5. Predicted total-system and individual-layer critical Rayleigh numbers vs fluid-layer thickness ratio, λ, with $L_3/L_1 = 0.96$, for a triple-air-layer system with Mylar intermediate barriers, along with experimental datum from test case 8 ($\lambda = 0.09$).

bers vs total-system temperature difference and a fluid-layer thickness ratio for double and triple air-layer systems.

To understand each of these figures, one might think of a multi-layer system with set fluid-layer thicknesses, and a given mean temperature and imposed temperature difference. Starting at a very low value, the pressure in the multi-layer system is gradually increased. The pressure and consequently the individual-layer and total-system Rayleigh numbers increase until the multi-layer system becomes unstable to infinitesimal disturbances. The individual-layer Rayleigh numbers and the total-system Rayleigh number at the onset of instability are the critical Rayleigh values shown in the figures. (This is exactly the procedure used in the experimental runs.) Figure 3 was then plotted by varying the imposed system temperature difference and Figs. 4 and 5 by varying the fluid-layer thickness ratio.

The first of these plots, Fig. 3, shows the individual-layer (solid and dashed lines) and total-system (dash-dotted line) critical Rayleigh numbers as functions of the total temperature difference for a double-air-layer system with a Teflon intermediate barrier. Figure 3 was plotted by increasing the temperature of the hot boundary while correspondingly decreasing the temperature of the cold boundary of the system so that the mean-system temperature remained constant at $T_M = 307$ K. The characteristics of the double-layer system used to produce Fig. 3 correspond to test-case 5 (see Table 1). Experimental data from test-case 5 are indicated with open circles on the plot.

In Fig. 4, individual layer (solid and dashed lines) and total-system (dash-dotted line) critical Rayleigh numbers for a double-layer system with a polyethylene inner barrier are plotted as functions of the fluid-layer thickness ratio, $\lambda = (L_2^3 - L_1^3)/L_{\max}^3$ (where $L_{\max}$ is the larger of L_1 and L_2). The plot represents the system stability while the placement of the intermediate barrier is shifted from a position at the upper boundary, $\lambda = -1$, through the middle of the total gap, $\lambda = 0$, and down to the lower boundary, $\lambda = +1$. The total-system gap width, mean temperature, and temperature difference chosen for the calculations were taken from the values given in Table 1 for test-case 6. A single datum from test-case 6 is shown with an open circle on the figure.

Figure 5 shows individual-layer (solid, dashed, and dotted lines) and total-system (dash-dotted lines) critical Rayleigh numbers vs the individual thickness ratio $\lambda = (L_2^3 - L_3^3)/L_{\max}^3$ (where $L_{\max}$ denotes the larger of L_2 and L_3) for the triple-layer system with Mylar intermediate barriers. Critical Rayleigh numbers were calculated for a range of the fluid-layer thickness ratio, λ, by starting with the two mylar intermediate barriers next to one another near the center of the stack ($\lambda = -1$) and then shifting them outward until they were adjacent to the outer boundaries ($\lambda = +1$). The ratio of thicknesses of the outer layers was held constant at $L_3/L_1 = 0.96$. The total-system gap width,

mean temperature, and temperature difference chosen for the calculations were taken from the values given in Table 1 for test-case 8. One datum from test-case 8 is indicated on the figure with an open circle.

DISCUSSION

Comparison of theory and experiment

Table 3 shows the comparison between theoretical predictions and experimental values of both critical Rayleigh number and subcritical Nusselt number. In every case the linear theory is seen to be in close agreement with the experimental measurements.

The first test case, a single layer with isothermal boundaries, was included in the experimental program to qualify the apparatus. The measured value of $Ra_{cr} = 1710$ is in excellent agreement with the well-known theoretical value of $Ra_{cr} = 1708$. In addition, the base-state heat-flux measurement is within 1% of that predicted from first principles. Both comparisons demonstrate the accuracy of the apparatus.

The agreement between measured and predicted critical Rayleigh numbers for the multi-layer systems is also excellent. In all of the multi-layer test cases listed in Table 3, except test-case 6, the linear theory predicts the results of the experimental runs within 4%. In test-case 6, the discrepancy between experiment and analysis is 8%. It is interesting to note that for all but one run, case 5b, measured critical Rayleigh numbers are slightly higher than the linear theory predicts.

In all cases, the predicted base-state heat flux is within 4% of the measured heat flux. Once again a trend is evident. For all but one case, test-case 1, the measured base-state heat fluxes are equal to or slightly less than the predicted heat fluxes.

Stabilizing effects of radiation and conduction

The stabilizing effect of radiative coupling to the intermediate barriers can be seen by reference to Table 3. The critical Rayleigh number predicted by a linear stability analysis which neglects boundary radiation is shown to the right of the prediction including radiation, as well as the per cent difference between the two predictions.

The addition of radiation is seen to increase the stability of all of the multi-layer test cases. However, the increase in critical Rayleigh number due to radiation is greatest for multi-layer systems with thin intermediate barriers of low conductivity (i.e. low values of H) and high emissivity. For example, in test-case 4, ignoring radiative coupling to the relatively high-emissivity, low H value, mylar intermediate barrier results in a value of critical Rayleigh number 11% lower than the more complete theory.

In multi-layer systems with high H, horizontal conduction dominates over radiative transfer as a stabilizing mechanism. Consider test-case 2 in which a double layer is divided by a phenolic intermediate barrier ($H = 1.2$, $\varepsilon = 0.9$), and test-case 3 in which a double layer is divided by a phenolic intermediate barrier covered with first-surface aluminized mylar ($H = 1.4$, $\varepsilon = 0.035$). The reduction in radiative coupling to the phenolic inner barrier due to the low-emissivity aluminized coating does reduce the double-layer's critical Rayleigh number. However, the change in critical Rayleigh number is small; the decrease is only about 2% for the theoretical numbers and 1% for the experimental numbers.

Comparing test-cases 2 and 3 with cases 4 and 5 shows the increase in multi-layer system stability associated with an increase in horizontal conduction in the intermediate barriers. Going from the double-layer systems with Mylar and Teflon inner barriers (cases 4 and 5) to the double-layer system with the phenolic inner barrier (cases 2 and 3) causes H to increase by a factor of about 100, and raises the measured system critical Rayleigh number from $Ra_{cr,tot} = 2.39 \times 10^4$ for the Mylar, and $2.25 \times 10^4 < Ra_{cr,tot} < 2.33 \times 10^4$ for the Teflon, to $Ra_{cr,tot} = 2.61 \times 10^4$, for the phenolic. The increase in critical Rayleigh number is a bit larger than 10%. Raising H further by replacing the phenolic barrier with an essentially isothermal sheet of copper ($H \to \infty$) would increase the system critical Rayleigh number only another 5%, to the theoretical maximum value of $Ra_{cr,tot} = 2.73 \times 10^4$.

Cross-over of individual-layer critical Rayleigh numbers

Inspection of Figs. 3, 4, and 5 reveals that the critical Rayleigh numbers for individual layers in a multi-layer system are generally not equal. For example, in Fig. 3 the individual-layer critical Rayleigh number for layer 1 is greater than that for layer 2 for total-system temperature differences below 25 K and is less for system temperature differences above 25 K. Only when the individual-layer critical Rayleigh numbers 'cross-over' at $\Delta T_{tot} = 25$ K is $Ra_{cr,1} = Ra_{cr,2}$. The location of the cross-over of individual-layer critical Rayleigh numbers is determined by the individual fluid-layer thicknesses, the temperature dependence of fluid thermophysical properties, and the temperature dependence imposed across each individual fluid layer.

Individual-layer Rayleigh number was previously defined in equation (6) in which all fluid properties were to be evaluated at the individual-layer mean temperature, $T_{M,i}$. For the air-filled systems of Figs. 3, 4, and 5, individual-layer Rayleigh number, Ra_i, will increase as ΔT_i and L_i increase and as $T_{M,i}$ decreases. The last assertion follows from the fact that both the conductivity and the dynamic viscosity of air are proportional to absolute temperature to the three fourths power ($K, \mu \propto T^{3/4}$) while both the volume coefficient of expansion and density of air are inversely proportional to temperature ($\rho, \beta \propto T^{-1}$). Therefore, since the Prandtl number of air is a weak function of temperature, the fluid-property dependence on mean-layer temperature will be roughly:

$$\beta_i/\nu_i^2 \propto T_{M,i}^{-4.5}. \quad (30)$$

It follows that in a multi-layer system of equal-thickness individual layers the cooler, upper air layers will be characterized by larger Rayleigh numbers than the hotter, lower air layers.

Radiative heat transfer will also cause the individual-layer Rayleigh numbers of equal-thickness layers in a multi-layer system to become unequal. In the case of a multi-layer system where all surfaces are of equal emissivity, the non-linear nature of radiative coupling between outer boundaries and inner barriers will act to shift the temperature of the inner barriers toward the hottest boundary in the multi-layer system. In a multi-layer system with surfaces of markedly different emissivities, the temperatures of inner barriers will tend to shift toward the temperatures of the highest emissivity surfaces. In both cases, shifts in intermediate barrier temperatures will cause individual-layer Rayleigh numbers to decrease in those layers where temperature differences decrease and increase where the temperature differences increase. For the case of multi-layer systems with equal-emissivity surfaces, thermal radiation will cause an effect similar to that of property temperature dependence, increasing the individual-layer Rayleigh numbers of the cooler, upper air layers over the hotter, lower layers. In general, the effects of both radiative heat transfer and fluid-property temperature dependence will grow as the total-system temperature difference increases.

Figures 3, 4 and 5 exemplify these points. The double air layer of Fig. 3 consists of two unequal-thickness individual layers ($L_1 > L_2$). This system would always have $Ra_{cr,1} > Ra_{cr,2}$ if property temperature dependence and thermal radiation were ignored. Accounting for these effects causes $Ra_{cr,2}$ to rise and $Ra_{cr,1}$ to fall as the total-system temperature difference increases. The cross-over in individual critical Rayleigh numbers occurs when:

$$(\beta_2 \Delta T_2)/\nu_2^2)/(\beta_1 \Delta T_1/\nu_1^2) = (L_1/L_2)^3. \quad (31)$$

Figure 3 shows that this condition is met at $\Delta T_{tot} = 25$ K.

Figure 4 demonstrates similar behavior. The individual-layer critical Rayleigh numbers for this double-layer system are only equal when layer 1 is thicker than layer 2 ($\lambda = -0.12$). When the two layers are of equal thickness, thermal radiation and property temperature dependence force the critical Rayleigh number of the cooler, upper layer to be significantly greater than the hotter, lower layer.

In the triple-layer system of Fig. 5, the cross-over of individual-layer critical Rayleigh numbers occurs when the inner air layer, layer 2, is larger than either of the outer air layers, layers 1 and 3 ($L_2 > L_1 \approx L_3$ or $\lambda = 0.54$). The inclusion of low-emissivity outer boundaries and high-emissivity inner barriers in the triple-layer system is responsible. Weak radiative coupling to the low-emissivity outer boundaries and strong radiative coupling between the two high-emissivity inner barriers causes the temperature difference across the inner layer to be smaller than the temperature differences across the outer layers. Consequently, individual-layer Rayleigh numbers can only be equal when the thickness of the inner layer is increased to compensate for the reduced temperature difference in accordance with equation (30).

Condition of maximum system stability

For the double-air-layer cases shown in Figs. 3 and 4, the total-system critical Rayleigh number reaches an absolute maximum directly above the cross-over of individual-layer critical Rayleigh numbers. The maximum occurs at $\Delta T_{tot} = 25$ K in Fig. 3 and at $\lambda = -0.12$ in Fig. 4. For the triple-air-layer case in Fig. 5, the maximum in total system critical Rayleigh number is shifted to a value of $\lambda = 0.47$, lower than the cross-over of individual-layer critical Rayleigh numbers at $\lambda = 0.54$.

The location of the maximum value of total-system critical Rayleigh number in Figs. 3, 4, and 5 can be understood by considering the condition of maximum stability for multi-layer stacks: maximum stability occurs in a multi-layer system when all individual layers reach the onset of instability simultaneously. The proof of this condition follows simply. Any convective motion within an unstable layer will create horizontal temperature gradients which will drive instabilities in neighboring fluid layers. Therefore, the total multi-layer system is only as stable as its least stable individual layer. Instability in a multi-layer system can be delayed by increasing the stability of less stable layers at the expense of decreasing the stability of more stable layers, until all layers become unstable simultaneously. Increasing the stability of a less stable layer can be accomplished, for example, by decreasing its thickness while correspondingly increasing the thickness of the more stable layers. (Note that varying λ in Figs. 4 and 5 produces this result. One individual layer's thickness is changed at the expense of the other individual layers' thicknesses while total-system thickness remains unchanged.)

The stability of an individual fluid layer is determined by the layer's thermal boundary conditions. It has previously been shown by Richards and Edwards [12] that the two thermal boundary conditions for any fluid layer can be characterized by two modified Biot numbers which account for both boundary conduction and radiation. The critical Rayleigh number and therefore the stability of a single layer increases monotonically as the Biot numbers characterizing either boundary increase.

Individual layers in a multi-layer system with equal Biot number boundaries will be equally stable and, in the absence of outside disturbances, will reach the onset of instability at equal critical Rayleigh numbers. Therefore, for a multi-layer system in which all individual layers have equal Biot-number boundaries, the

condition of maximum stability implies that the total system will be most stable when all of the individual-layer critical Rayleigh numbers are equal ($Ra_{cr,i} = Ra_{cr,j}$ for all i and j). Figures 3 and 4 exemplify this point. Each of the double-layer systems used to construct the figures are composed of individual layers with symmetric thermal boundary conditions ($Bi_{inner} \approx 1$, $Bi_{outer} \to \infty$). The two layers in each system are equally stable, and consequently the point of maximum system stability occurs at the cross-over of individual-layer critical Rayleigh numbers.

In contrast, in a multi-layer system with individual fluid layers characterized by unequal Biot numbers, the individual layers will not be equally stable. The condition of maximum stability implies that the total system will be most stable when the individual-layer critical Rayleigh numbers are not equal. Maximum system stability will occur when the more stable individual layers with high-Biot-number boundaries have higher critical Rayleigh numbers than the less stable layers with low-Biot-number boundaries. This behavior can be seen in the triple-layer system of Fig. 5. The two outer fluid layers, layers one and three, are symmetric, each with one high- and one low-Biot-number boundary ($Bi_{inner} \approx 1$, $Bi_{outer} \to \infty$). The inner fluid layer, layer two, has two low-Biot-number boundaries ($Bi_{top} \approx 1$, $Bi_{bottom} \approx 1$). The inner fluid layer is consequently the least stable of the three layers. Maximum system stability will therefore occur when the critical Rayleigh number for layer two is smaller than the critical Rayleigh numbers for layers one and three ($Ra_{cr,2} < Ra_{cr,1} \approx Ra_{cr,3}$). Fig. 5 confirms this assertion.

SUMMARY

A linear perturbation analysis accounting for boundary radiation has been applied to the problem of thermal stability in a multi-layer stack. Heat-flux measurements in single, double, and triple air layers using a guard heated calorimeter confirm the results of the theory. Measured critical Rayleigh numbers agree with theoretical predictions to within 4% for eight out of the nine test cases run. Major conclusions of the study are:

1. Both radiative coupling to intermediate barriers and horizontal conduction in the barriers act to stabilize multi-layer systems.
2. Radiative coupling and fluid-property temperature dependence, in general, cause the colder layers higher up in a multi-layer stack to shift to higher Rayleigh numbers than lower and hotter layers of equal thickness. Radiation heat transfer may also cause the temperatures of high-emissivity intermediate barriers to shift toward one another, causing the Rayleigh numbers for the layers between those barriers to decrease.
3. The most stable configuration for a multi-layer stack occurs when all individual layers reach the onset of instability simultaneously. In multi-layer systems made up of individual fluid layers characterized by equal Biot numbers, maximum stability occurs when the individual-layer critical Rayleigh numbers are equal. In multi-layer systems made up of individual layers characterized by unequal Biot numbers, maximum system stability occurs when the more stable (high-Biot-number) layers have larger individual-layer critical Rayleigh numbers than the less stable (low-Biot-number) layers.

Acknowledgements—The author wishes to thank Professor D. K. Edwards of the University of California, Irvine for his generous advice throughout the course of this work. The contributions of Mr J. H. Chung of Tayco Engineering, Inc. toward the construction of the experimental apparatus are gratefully acknowledged.

REFERENCES

1. A. Whillier, Plastic covers for solar collectors, *Sol. Energy* **7**, 148–151 (1963).
2. K. G. T. Hollands and J. L. Wright, Heat loss coefficients and effective $\tau\alpha$ products for flat-plate collectors with diathermanous covers, *Sol. Energy* **30**, 211–216 (1983).
3. K. G. T Hollands, T. E. Unny, G. D. Raithby and L. Konicek, Free convection heat transfer across inclined air layers, *ASME J. Heat Transfer* **98**, 189–193 (1976).
4. D. K. Edwards and S. J. Rhee, Nongray-radiative and convective–conductive thermal coupling in Teflon-glazed, selective-black, flat-plate solar collectors, *Sol. Energy* **30**, 211–216 (1983).
5. E. M. Sparrow, R. J. Goldstein and V. K. Jonsson, Thermal instability in a horizontal fluid layer: effect of boundary conditions and non-linear temperature profile, *J. Fluid Mech.* **18**, 513–528 (1964).
6. G. V. Gershuni and E. M. Zhukovitskii, Convective stability of incompressible fluids, Israel Program for Scientific Translations, Jerusalem (1976).
7. I. Catton and J. H. Lienhard, V, Thermal stability of two fluid layers separated by a solid interlayer of finite thickness and thermal conductivity, *ASME J. Heat Transfer* **106**, 605–612 (1984).
8. J. H. Lienhard V and I. Catton, Heat transfer across a two-fluid-layer region, *ASME J. Heat Transfer* **108**, 198–205 (1986).
9. T. R. Ulrich, Heat transfer across a multi-layered air enclosure, M.S. Thesis, University of California, Irvine, CA (1984).
10. J. H. Lienhard V, An improved approach to conductive boundary conditions for the Rayleigh–Benard instability, *ASME J. Heat Transfer* **109**, 378–387 (1987).
11. C. A. Hieber, Multilayer Rayleigh–Bénard instability via shooting method, *ASME J. Heat Transfer* **109**, 538–540 (1987).
12. R. F. Richards and D. K. Edwards, Effect of boundary radiation on thermal stability in horizontal layers, *Int. J. Heat Mass Transfer* **32**, 81–86 (1989).
13. J. H. Lienhard V, Thermal radiation in Rayleigh Bénard instability, *ASME J. Heat Transfer* **112**, 100–109 (1990).
14. S. Chandrasekhar, *Hydrodynamic and Hydromagnetic Stability*, pp. 9–73. Clarendon Press, Oxford (1961).
15. D. K. Edwards, The plating algorithm for radiation script-F transfer factor, *ASME J. Heat Transfer* **108**, 237–238 (1986).
16. R. F. Richards, Thermal stability in stacked horizontal fluid layers with partially transparent boundaries, Ph.D. Thesis, University of California, Irvine, CA (1990).
17. N. B. Vargaftik, *Tables of Thermophysical Properties of Liquids and Gases*, 2nd Edn, pp. 200–250. Hemisphere, New York (1975).